Analyst

ROYAL SOCIETY OF CHEMISTRY

PAPER

View Article Online
View Journal | View Issue

Cite this: *Analyst*, 2022, **147**, 398

Ultrasensitive detection of vitamin E by signal conversion combined with core-satellite structure-based plasmon coupling effect†

Keying Xu,[a] Jing Li,[a] Qingyi Han,[a] Dingding Zhang,[a] Libing Zhang,[a] Zhen Zhang *[a] and Xiaoquan Lu *[b]

Received 19th December 2021,
Accepted 4th January 2022

DOI: 10.1039/d1an02289j

rsc.li/analyst

The rapid and sensitive surface-enhanced Raman scattering (SERS) detection of molecular biomarkers from real samples is still a challenge because the intrinsically trace analytes may have a low molecular affinity for metal surfaces. Herein, we develop a smart signal conversion and amplification strategy based on silver–gold–silica core-satellite structure nanoparticles (Ag@Au@SiO_2 NPs) to sensitively detect low adsorptive vitamin E using SERS, which has been considered a biomarker of neuromuscular disorders when its abnormal content is measured in the serum of patients. Through the reducibility of vitamin E, Ag^+ ions are rapidly reduced to Ag atoms, resulting in the epitaxial growth of Ag nanocrystals on gold nanoparticles forming satellite particle–particle gap-narrowed Ag@Au@SiO_2 NPs. The generated strong plasmonic field dramatically enhances the Raman signal of the Raman reporter molecule 4-aminothiophenol (4-ATP) and the detected vitamin E molecules at an estimated level of 58.19 nmol L^{-1}. The sensitivity of this operational SERS strategy provides tremendous prospects for the screening of neuromuscular disorders.

1. Introduction

The rapid and sensitive detection of molecular biomarkers from body fluids, such as urine, saliva, phlegm, and blood, is of great significance in understanding the physiological and pathological states of an individual and provides an important strategy for disease diagnosis and monitoring.[1] Currently, general analytical techniques, such as gas chromatography (GC),[2,3] gas chromatography-mass spectrometry (GC-MS),[4,5] colorimetry,[6] and fluorescence spectrometry, have been employed to measure biomarkers.[7,8] A challenge arises when it comes to detecting low concentrations of biomarkers in body fluids, wherein the biomarkers are generally submerged or contained in diverse chemical compositions and even biomacromolecules.[9–11]

To achieve the goal of ultra-sensitively detecting and monitoring biomarkers, a promising alternative detection approach has been developed with the aim of amplifying the detectable signal *via* adopting innovative and powerful signal generation tags.[12–15] Recently, several sensing schemes, such as photoelectron chemical (PEC) assays,[16,17] resonance light scattering (RLS) technology,[18–21] and SERS, have been investigated to obtain the target molecular information.[22–24] Among all of them, with the surface plasmon phenomena of noble metal nanostructures, SERS is considered the most ideal technique that provides fingerprint vibrational information with ultra-high sensitivity, specificity, and anti-interference capability.[25] For example, Wu *et al.* designed SERS probes with Au nanostar@Raman reporter@silica sandwich nanoparticles to ultrasensitively detect the neuron-specific enolase (NSE) biomarker in blood plasma *via* the Au nanostar, which generates a strong plasmonic field to amplify the SERS signal of the Raman reporter molecules.[26] In our previous work, we combined a bionic antenna structure with the pregrafted Raman-active probe molecule 4-ATP for the SERS detection of gaseous molecules, where gaseous aldehyde molecules flowing in the dendritic surface could participate in a sufficient nucleophilic addition reaction with 4-ATP.[27] Notably, such sensitive detection of analytes commonly requires sensing schemes where the target molecules are absorbed on a SERS substrate or by chemical bonding. The process of absorption and chemical bonding, therefore, is critical to the detection limit of the analytes. However, these may not exhibit impressive performance in detecting low-concentration molecular markers because many biomarkers are Raman weak and are hardly absorbed or fixed on solid substrates. A classic example is vitamin E, which is present in levels above 1.16 mmol L^{-1} in serum, and has

[a]*Tianjin Key Laboratory of Molecular Optoelectronic, Department of Chemistry, School of Science, Tianjin University, Tianjin, 300072, P. R. China. E-mail: zhzhen@tju.edu.cn*
[b]*Key Laboratory of Bioelectrochemistry & Environmental Analysis of Gansu Province, College of Chemistry & Chemical Engineering, Northwest Normal University, Lanzhou, 730070, P. R. China. E-mail: luxq@nwnu.edu.cn*

†Electronic supplementary information (ESI) available. See DOI: 10.1039/d1an02289j

been identified as a biomarker for neuromuscular disorders (including spinal cerebellar syndrome with peripheral nerve involvement and Alzheimer's disease).[28,29] Recently, GC,[30] fluorescence detection (FLD),[31] GC-MS,[32] and electrochemical methods[33] have been used to detect vitamin E. However, the general analytical methods generally require complex analytical procedures or time-consuming processes and yield insensitive detection. Therefore, it is highly desirable to design a convenient, highly sensitive, and selective analytical strategy for determining vitamin E in complex biological systems.

Unlike prior methods, this article reports a smart signal conversion and amplification concept to design a silver–gold–silica core-satellite nanostructure, amplifying the Raman signal of the Raman reporter molecules for the SERS detection of vitamin E. Herein, the signal nano-transducer of gold–silica core-satellite nanoparticles (Au@SiO_2 NPs) were synthesized by the *in situ* growth of gold nanoparticles on silica dioxide nanoparticle cores. Due to the close match of lattice constants (f = 0.2%), the dispersed gold nanoparticles can readily act as heterogeneous nucleation sites for the fast epitaxial growth of silver nanocrystals.[34] When vitamin E is present in the alkaline solution, their phenolic groups convert to a quinone structure, which rapidly reduces Ag^+ ions to Ag atoms, forming satellite particle–particle gaps (*i.e.*, hotspots) narrowed Ag@Au@SiO_2 NPs. With the generated strong plasmonic field, the Raman signal of 4-ATP, which was chosen as the Raman reporter molecule, is dramatically amplified and realizes the signal conversion and indirect detection of vitamin E molecules at a level of nmol L^{-1}. This SERS detection based on the plasmon coupling effect using the concept of signal conversion and amplification has the characteristics of being fast, easy, and cost-effective, which has obvious potential in biological applications for vitamin E-associated disease monitoring and clinical diagnostics.

2. Experimental

2.1 Synthesis of NH_2-functionalized SiO_2 NPs

The SiO_2 spheres were prepared following the improved Stöber method.[35] Firstly, 2.3 mL tetraethyl orthosilicate (TEOS) was mixed with 60 mL ethanol, and 1 mL water and 3 mL ammonia solution were then added. After stirring for 6 h at 25 °C, the products were centrifuged, washed with ethanol and water, and then dried to obtain SiO_2 solid. Lastly, 100 μL (3-aminopropyl) triethoxysilane (APTES) was added to the SiO_2 dispersion (10 mL, 10 mg mL^{-1}), and the reaction solution was stirred for 12 h at 25 °C to obtain NH_2-functionalized SiO_2 NPs (NH_2-SiO_2 NPs).

2.2 Synthesis of Au@SiO_2 NPs

Au@SiO_2 NPs were synthesized by the *in situ* growth method.[36] Briefly, NH_2-SiO_2 powder (200 mg) was dispersed in 20 mL water to form a uniform solution. Subsequently, gold(III) chloride trihydrate solution ($HAuCl_4$) (2.0 mL, 20 mmol L^{-1}) was added slowly into the NH_2-SiO_2 solution. After that, freshly prepared sodium borohydride solution ($NaBH_4$) (30 mL, 10 mmol L^{-1}) was added to the above mixed solution and reacted for 3 h at 25 °C. Finally, the resultant Au@SiO_2 NPs were washed with ethanol and water three times and redispersed in 10 mL ethanol for further use.

2.3 Synthesis of Ag@Au@SiO_2 NPs

Ag@Au@SiO_2 NPs were synthesized by reducing $AgNO_3$ with vitamin E in the presence of polyvinyl pyrrolidone (PVP). Briefly, the previously synthesized Au@SiO_2 NPs were dispersed in a 700 μL PVP solution. 100 μL silver nitrate solution ($AgNO_3$) and 10 μL sodium hydroxide (NaOH) were added to the solution. The reaction solution was heated at 37 °C for 3 min, after which 100 μL vitamin E solution was added to the solution and maintained for 1 h at 37 °C until a brown solution was formed. Finally, Ag@Au@SiO_2 NPs were obtained by centrifugation and washed with ethanol to remove the excess solvent in the system. The obtained Ag@Au@SiO_2 NPs were redispersed in ethanol.

2.4 SERS detection of vitamin E

The SERS spectra were collected using a Thermo Fisher Raman spectrometer (DXR2xi, USA). The excitation wavelength was 532 nm and the exposure time was 2 s. 4-ATP was selected as a standard Raman reporter to detect vitamin E. The Raman peaks of 4-ATP at 1079, 1136, 1436 and 1571 cm^{-1} could be observed by SERS. Briefly, 5 μL of Ag@Au@SiO_2 NPs were dropped vertically onto a clean glass sheet, followed by the addition of 5 μL 4-ATP (10 mmol L^{-1}) after the sample was completely dried to collect the SERS signal.

2.5 Finite-different time-domain (FDTD) simulation

The FDTD simulation calculations were performed by FDTD solutions (version 8.15736, Lumerical Solutions, Inc., USA) to simulate the electric-field energy density distribution of the Ag@Au@SiO_2 NPs. The illumination source was a Bloch/periodic plane-wave of wavelength 900 nm with z-axis injection and an amplitude of 1. The mesh type was uniform. Periodic boundary conditions were set for the x and y directions, and perfectly matched layer boundary conditions were set for the z-direction. A monitor was set behind the plane-wave source to ensure the correct measurement of the reflected waves. Time monitors were added to exhibit the light evolution inside the models. A cross-sectional electric field monitor was placed at the cross-section plane to analyze the electric field intensity distribution inside the models. The nanoparticle sizes and shapes in the FDTD simulations were obtained from transmission electron microscopy (TEM) images.

3. Results and discussion

3.1 Design and synthesis of Ag@Au@SiO_2 NPs

SERS is a highly sensitive and specific sensing technique in which Raman signals of analyte molecules are greatly enhanced by several orders of magnitude when the analytes

are adsorbed at or very close to nanostructured noble metal surfaces such as Ag and Au. It is generally considered that the Raman signal enhancement mainly depends on the amplification of the local electromagnetic (EM) fields associated with the plasmon excitation in the noble metal. According to classical electromagnetism, the corresponding SERS enhancement can be well evaluated in the $|E|^4$-approximation, where E is the local electric field intensity.[37] As the electric field strength depends strongly on the gap distance, the EM field amplitude has an approximate inverse gap dependence, resulting in the extension of a typical SERS hotspot lying in the 2–10 nm range.[38,39] Therefore, specific and accurate manipulation of the nano-sized hotspots *via* well-designed Ag or Au nanostructures is crucial for achieving ultrahigh SERS intensity. The synthesized nanostructures act as active substrates for SERS detection, while the synthesis process also provides a potential method for molecular detection. In particular, the molecule involved in a synthesis process directly influences the local electric field intensity by controlling noble metal nanostructures. This unique characteristic of the molecule results in electromagnetically enhanced signals *via* the "nano-transducer", enabling the sensitive SERS detection of the corresponding molecule.

The fabrication of the smart plasmonic nano-transducers and their SERS sensing mechanism is schematically illustrated in Scheme 1. Au@SiO_2 NPs were synthesized by the *in situ* growth of gold nanoparticles on SiO_2 nanoparticle (SiO_2 NP) cores. In the alkaline ethanol solution, since the phenolic groups of vitamin E can be easily oxidized into quinone structures, vitamin E shows strong reducibility, which can transfer electrons to Ag^+ ions for the formation of Ag atoms. As the lattice mismatch factor between Au and Ag is 0.2%, the obtained Ag atoms in the solution prefer to epitaxially grow on the surface of the Au "seed". The growth of core-satellite structures can be achieved by tuning the synthesis parameters such as $AgNO_3$ concentration, NaOH concentration, and reaction time. After the injection of $AgNO_3$ solution, a characteristic absorption peak appearing around 423 nm in the ultraviolet-visible absorption (UV-vis) spectrum suggests that the uniform growth of the Ag shell on top of the gold satellite/nanoparticles (Au NPs) effectively modulates the plasmonic properties of the Ag@Au@SiO_2 NPs. With the increase of $AgNO_3$ concentration, the peak at 423 nm of the optical response reaches the maximum value at 10 mmol L^{-1}, matching well with the generated core-satellite structures where the NPs are uniformly distributed on the Au NPs (Fig. 1a), while further increasing the Ag precursor causes a decline of the peak at 423 nm. This result is due to the Ag atoms growing into large Ag NPs and the satellite particles growing big and irregular crystals on the SiO_2 NPs (Fig. S1†).[40] It is also found that NaOH concentration and reaction time would affect the formation of core-satellite structures. An investigation into the synthesis of Au@Ag@SiO_2 NPs at different NaOH concentrations and reaction times was conducted. As shown in Fig. 1b and c, when the NaOH concentration is 40 mmol L^{-1} and the reaction time is 60 min, the characteristic absorbance near 423 nm in the UV-vis absorption spectra reached the maximum (Fig. S2 and S3†), indicating the fabrication of uniform and well-defined Ag@Au@SiO_2 NPs.

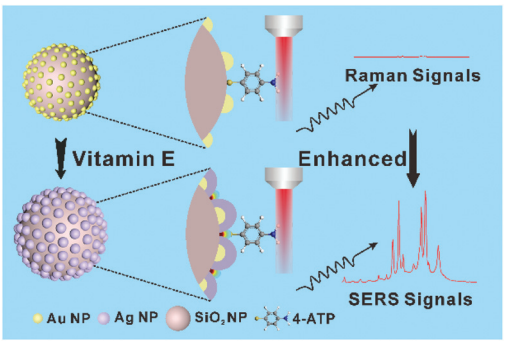

Scheme 1 Schematic illustration of the detection process.

3.2 Characterization of Ag@Au@SiO_2 NPs

The morphology and synthesis intermediates of the Ag@Au@SiO_2 NPs are shown in Fig. 1d and Fig. S5, S6.† The outer surface of the SiO_2 NPs was firstly modified with amino groups by introducing APTES, following by the *in situ* growth of Au NPs to produce well-defined Au@SiO_2 NPs. The Fourier transform infrared (FT-IR) spectra shows that the presence of $-NH_2$ groups on the surface of SiO_2 NPs provides a large number of Au NP anchoring sites (Fig. S4†). The diameter of the SiO_2 core is 85 nm (Fig. S5†) and the diameter of the Au NPs is about 6 nm (Fig. S6†). Then, Ag NPs epitaxially grow on the outer surface of the Au NPs to produce Ag@Au@SiO_2 NPs. The fabricated Ag@Au@SiO_2 NPs consist of large numbers of satellite nanoparticles with a mean diameter of 10.5 nm (Fig. S7†), as shown in the HRTEM of Fig. 1d. During the reac-

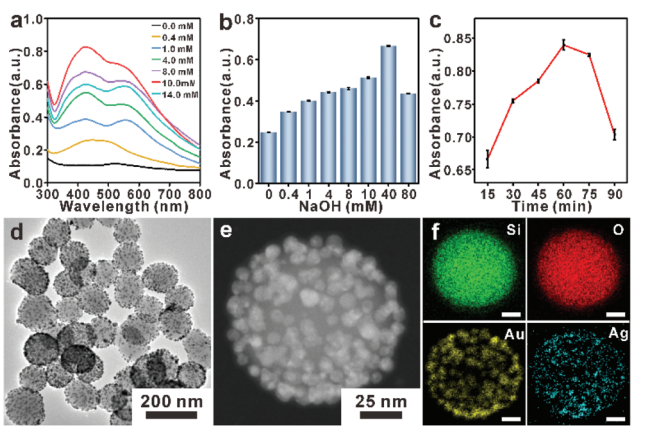

Fig. 1 (a) UV-vis spectra of the Ag@Au@SiO_2 NPs at different $AgNO_3$ concentrations ranging from 0 mmol L^{-1} to 14 mmol L^{-1}. (b) Histogram of the Ag@Au@SiO_2 NPs with increasing NaOH concentration. (c) Line chart of the Ag@Au@SiO_2 NPs at different times. (d) High-resolution transmission electron microscopy (HRTEM) image of the Ag@Au@SiO_2 NPs. (e and f) Elemental mapping images of Si, O, Au and Ag in the Ag@Au@SiO_2 NPs. Scale bars in (f) are 10 nm.

tion, Ag atoms aggregate to grow along the Au NP surface, which is proved by the UV-vis spectrum. As shown in Fig. S8,† the characteristic absorption peaks of Au NPs (523 nm) and Ag NPs (423 nm) appear simultaneously in the UV-vis spectra of the Ag@Au@SiO_2 NPs. The HRTEM image collected from the satellite structure (Fig. S9†) clearly displays lattice spacings of 0.236 nm and 0.206 nm, which are consistent with the (111) planes and (001) planes of the face-centered cubic (fcc) structure. They could be considered as a metal alloy of Ag and Au atoms.[41,42] The images of elemental mapping (Fig. 1e and f) show strong Au and Ag signals within uniform regions on the SiO_2 surface, which further confirms the successful fabrication of the Ag@Au@SiO_2 NPs. The XPS spectra of the Ag@Au@SiO_2 NPs in Fig. S10 and S11† reveal that both Au and Ag existed in the metallic state, which is consistent with previous reports in the literature.[43,44]

3.3 Electromagnetic field enhancement

To better explore the geometric structure of nanogaps and the SERS enhancement mechanism, the FDTD method was employed to study the electric field distribution for the Au@SiO_2 NPs and Ag@Au@SiO_2 NPs using the software for FDTD solutions. Characterized by many nanometer-sized intra-satellite gaps on the surface of the SiO_2 core, the Ag@Au@SiO_2 NPs exhibit dramatically increased local electromagnetic fields. The simulations were constructed according to the TEM and HRTEM images under optimal conditions. As depicted from the *x*–*y* view of the electric field distribution, hot spots are densely distributed in the two simulation models (Fig. 2a and b).

The localized electromagnetic field intensity at the Ag@Au@SiO_2 NPs ($E_1 \approx 126$) is much stronger than at the Au@SiO_2 NPs ($E_2 \approx 30$). Obviously, the local electromagnetic field shows a strong plasmon resonance effect benefiting from the hot spot effect near/within the nanogaps between adjacent satellite NPs on the Ag@Au@SiO_2 NPs (Fig. 2c). The simulated enhancement factor (EF) for the Ag@Au@SiO_2 NPs under excitation is estimated to be 1.59×10^4 using the EF $\propto |E|^4$ approximation, which is much higher than that of the Au@SiO_2 NPs, demonstrating the critical role of the narrowed nanogap distance with the strong electromagnetic field. This reductant molecule-induced signal/electromagnetic field amplification strategy can be used for the detection of the corresponding reductant molecules.

3.4 SERS detection of vitamin E

The SERS performance and stability of Ag@Au@SiO_2 NPs as a substrate were evaluated. The signal intensity of the Raman spectrum of these Ag@Au@SiO_2 samples enhances significantly, implying the large Raman enhancement of the Ag@Au@SiO_2 core-satellite structure. Typically, with 100 μmol L^{-1} of 4-ATP, the characteristic Raman peak intensity at 1079 cm^{-1} is enhanced about 600 times and 200 times compared to that of the blank SERS base and Au@SiO_2 NPs, respectively (Fig. 2d). The calculated EF is as high as 1.6×10^5 (details are shown in the ESI†). It is lower than the simulated enhancement factor of a single Ag@Au@SiO_2 NP (at 633 nm), which might be attributed to the charge transfer between 4-ATP and the substrate surface.[37] The Raman peak intensity on the Ag@Au@SiO_2 NPs exhibits good signal reproducibility. The corresponding relative standard deviation (RSD) value of the 4-ATP peak intensity at 1079 cm^{-1} is about 5.26%, obtained by comparing 15 independent SERS spectra collected from different spots at the Ag@Au@SiO_2 NPs (Fig. 2e and f).

To investigate the feasibility of the signal conversion and electromagnetic field amplification concept for the SERS detection of vitamin E, the Raman-active probe molecule 4-ATP was selected and recorded (Fig. 3), wherein the Raman characteristic peak intensity is controlled by the topology of the core-satellite structure. To quantitatively evaluate the existence of vitamin E, the SERS spectra of 4-ATP (10 mmol L^{-1}) were collected as a function of vitamin E concentration from 0.1 to 180 μmol L^{-1}. As shown in Fig. 3a, the main characteristic Raman bands that are located at 1079, 1136, 1436, and

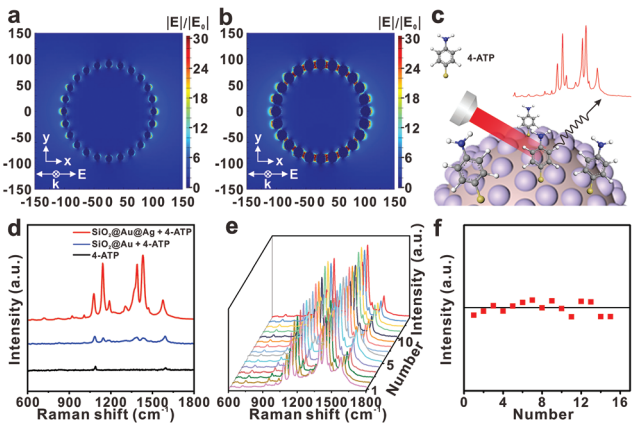

Fig. 2 FDTD simulations of the EM field distribution of (a) Au@SiO_2 NPs and (b) Ag@Au@SiO_2 NPs. (c) Schematic diagram of the detection process of 4-ATP as a Raman reporter molecule. (d) SERS spectra of blank, Au@SiO_2 and Ag@Au@SiO_2 NPs used as the nano-transducer when 4-ATP was used as a Raman reporter. (e) Corresponding to the SERS intensity distribution at 1079 cm^{-1}. (f) SERS spectra of 10 mmol L^{-1} 4-ATP measured at 15 different points on the Ag@Au@SiO_2 NPs nano-transducer randomly selected.

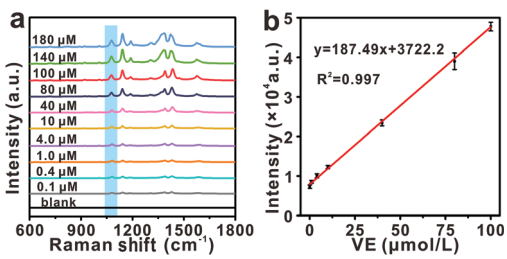

Fig. 3 (a) SERS spectra of 4-ATP in the presence of vitamin E with different concentrations (from 0.1 μmol L^{-1} to 180 μmol L^{-1}). (b) The calibration curve between the Raman intensity response obtained at 1079 cm^{-1} and different concentrations of 4-ATP (from 0.1 μmol L^{-1} to 100 μmol L^{-1}).

Table 1 Determination of vitamin E concentration in human serum samples

Serum sample[a]	Add (μmol L^{-1})	Found (μmol L^{-1})	Recovery (%)	RSD (%) $N = 3$
1	10	9.51	95.10	3.29
		9.47	94.70	
		10.04	100.40	
2	20	20.96	104.80	4.33
		19.49	97.45	
		19.44	97.20	

[a] The real serum samples were obtained from the First Teaching Hospital of Tianjin University of Traditional Chinese Medicine, Tianjin.

1571 cm^{-1} are consistent with previously reported experimental and theoretical results. The strength of the Raman signal collected from the Ag@Au@SiO_2 NPs weakens gradually with the decrease of vitamin E concentration, but the Raman signal is still clearly recognized even at a concentration of 0.1 μmol L^{-1}. The Raman peak intensity shows a linear rise with an increasing concentration of vitamin E until 100 μmol L^{-1}. Typically, the Raman intensity of 1079 cm^{-1} (I_{1079}) has a linear relationship (R^2 = 0.997) with the concentration of vitamin E (Fig. 3b). The detection limit ($3\sigma/k$) for vitamin E is 58.19 nmol L^{-1}, much lower than the normal vitamin E level in the human body. Additionally, the detection method exhibits a high degree of anti-interference, largely due to the specific alkaline ethanol reaction system. The selectivity of this platform was evaluated by examining other potential interfering factors, including common proteins and amino acids in serum, like lysine (Lys), histidine (His), phenylalanine (Phe), L-cysteine (Cys), and valine (Val). As shown in Fig. S12,† except for vitamin E, the characteristic Raman peak intensity at 1079 cm^{-1} for other analytes displayed no apparent enhancement.

3.5 Detection of vitamin E in the serum samples

To assess the applicability of this newly developed strategy for real samples, different concentrations of vitamin E (10 μmol L^{-1} and 20 μmol L^{-1}) were added to diluted serum samples as models for the detection of real samples. The SERS spectra and statistical analysis of the peak intensity at 1079 cm^{-1} can be obtained in Table 1. The measured vitamin E concentration is close to the actual concentration. The average recovery of vitamin E and the RSD were calculated to quantitatively evaluate the performance of the method. As shown in Table 1, the measured concentration of vitamin E is close to the standard concentration, and the recovery is from 94.70% to 104.80%. These results indicate that the proposed detection system possesses good reliability for the detection of vitamin E in clinical applications.

4. Conclusions

In summary, this work demonstrates an innovative Raman signal conversion and amplification strategy for the ultrasensitive and selective detection of molecular markers by synthesizing a Ag@Au@SiO_2 NP nano-transducer. Benefitting from the epitaxial growth of Ag nanocrystals on gold nanoparticles *via* the reduction reactions between vitamin E and Ag^+ ions, the strong plasmonic field generated by the narrowing of the satellite particle–particle gap is significantly enhanced, and the vitamin E signal converted to the intense Raman signal of the Raman reporter molecule 4-ATP, overcoming the long-standing limitation wherein the analyte molecule should absorb or fix on a surface for SERS detection. Through the strong surface plasmon resonance generated from the Ag@Au@SiO_2 NPs, the Raman signal of 4-ATP exhibits a remarkable change to afford the detection limit of vitamin E at the nmol L^{-1} level. With the capability of selective and sensitive SERS detection of vitamin E from serum, this strategy has an observable potential in the diagnosis of preclinical neuromuscular disorders and reliable point-of-care tests. Our study details also provide a deeper understanding and insight into the signal conversion and amplification concept, which will direct the design of other analyte molecule detection methods.

Author contributions

Keying Xu: designed, characterized, and SERS analyzed the samples. Jing Li, Qingyi Han, Dingding Zhang, and Libing Zhang: helped in the analysis, paper drafting, and reviewed the paper. Zhen Zhang and Xiaoquan Lu: supervised, reviewed the writing, and provided funding acquisition. All authors contributed to the general discussion.

Conflicts of interest

There are no conflicts to declare.

Acknowledgements

This work was supported by the National Natural Science Foundation of China (no. 21705117, 21904095, and 22004089), the Program of Tianjin Science and Technology Major Project and Engineering (19ZXYXSY00090), the Program for Chang Jiang Scholars and Innovative Research Team, Ministry of Education, China (IRT-16R61), and the Special Fund Project for the Central Government to Guide Local Science and Technology Development (2020).

Notes and references

1 Y. Y. Broza, X. Zhou, M. Yuan, D. Qu, Y. Zheng, R. Vishinkin, M. Khatib, W. Wu and H. Haick, *Chem. Rev.*, 2019, **119**, 11761–11817.
2 J. S. Zavahir, Y. Nolvachai and P. J. Marriott, *TrAC, Trends Anal. Chem.*, 2018, **99**, 47–65.

3 A. Venkatasubramanian, V. T. Sauer, S. K. Roy, M. Xia, D. S. Wishart and W. K. Hiebert, *Nano Lett.*, 2016, **16**, 6975–6981.
4 J. W. Sen, H. R. Bergen and N. H. Heegaard, *Anal. Chem.*, 2003, **75**, 1196–1202.
5 H. Kang, X. Li, Q. Zhou, C. Quan, F. Xue, J. Zheng and Y. Yu, *Br. J. Dermatol.*, 2017, **176**, 713–722.
6 J. Li, J. Zhao, S. Li, Y. Chen, W. Lv, J. Zhang, L. Zhang, Z. Zhang and X. Lu, *Nano Res.*, 2021, **14**, 4689–4695.
7 L. Zhang, C. J. Sevinsky, B. M. Davis and A. Vertes, *Anal. Chem.*, 2018, **90**, 4626–4634.
8 X. Tian, B. Xie, Z. Zou, Y. Jiao, L. Lin, C. Chen, C. C. Hsu, J. Peng and Z. Yang, *Anal. Chem.*, 2019, **91**, 12882–12889.
9 Y. Kao, X. Han, Y. H. Lee, H. Lee, G. C. Phan-Guang, C. L. Lay, H. Y. F. Sim, V. J. X. Phua, L. S. Ng, C. W. Ku, T. C. Tan, I. Y. Phang, N. S. Tan and X. Y. Ling, *ACS Nano*, 2020, **14**, 2542–2552.
10 E. Er, A. Sánchez-Iglesias, A. Silvestri, B. Arnaiz, L. M. Liz-Marzán, M. Prato and A. Criado, *ACS Appl. Mater. Interfaces*, 2021, **13**, 8823–8831.
11 Y. Wang, Y. Hou, H. Li, M. Yang, P. Zhao and B. Sun, *Microchim. Acta*, 2019, **186**, 548.
12 Z. Yu, G. Cai, X. Liu and D. Tang, *Anal. Chem.*, 2021, **93**, 2916–2925.
13 S. Lv, K. Zhang, L. Zhu and D. Tang, *Anal. Chem.*, 2019, **92**, 1470–1476.
14 L. Huang, J. Chen, Z. Yu and D. Tang, *Anal. Chem.*, 2020, **92**, 2809–2814.
15 J. Shu and D. Tang, *Anal. Chem.*, 2019, **92**, 363–377.
16 X. Guan, X. Deng, J. Song, X. Wang and S. Wu, *Anal. Chem.*, 2021, **17**, 6763–6769.
17 J. Zhuang, B. Han, W. Liu, J. Zhou, K. Liu, D. Yang and D. Tang, *Biosens. Bioelectron.*, 2018, **99**, 230–236.
18 S. Yan, D. Deng, H. Song, Y. Su and Y. Lv, *Sens. Actuators, B*, 2017, **243**, 873–881.
19 Z. Chen, Y. Lei and X. Chen, *Microchim. Acta*, 2012, **179**, 241–248.
20 M. Amjadi and A. Samadi, *J. Food Drug Anal.*, 2011, **19**, 4.
21 H. Wen, H. Wang, J. Hai, S. He and F. Chen, *ACS Sustainable Chem. Eng.*, 2019, **7**, 5200–5208.
22 P. Li, M. Ge, C. Cao, D. Lin and L. Yang, *Analyst*, 2019, **144**, 4526–4533.
23 O. Guselnikova, Y. Kalachyova, K. Hrobonova, M. Trusova, J. Barek, P. Postnikov, V. Svorcik and O. Lyutakov, *Sens. Actuators, B*, 2018, **265**, 182–192.
24 S. Kamal and T. C.-K. Yang, *J. Colloid Interface Sci.*, 2022, **605**, 173–181.
25 J. Li, Y. Huang, Y. Ding, Z. Yang, S. B. Li, X. S. Zhou, F. R. Fan, W. Zhang, Z. Zhou, D. Wu, B. Ren, Z. Wang and Z. Tian, *Nature*, 2010, **464**, 392–395.
26 X. Gao, P. Zheng, S. Kasani, S. Wu, F. Yang, S. Lewis, S. Nayeem, E. B. Engler-Chiurazzi, J. G. Wigginton, J. W. Simpkins and N. Wu, *Anal. Chem.*, 2017, **89**, 10104–10110.
27 Z. Zhang, W. Yu, J. Wang, D. Luo, X. Qiao, X. Qin and T. Wang, *Anal. Chem.*, 2017, **89**, 1416–1420.
28 K. H. Chan, M. O'Sullivan, I. Farouji, G. Are and J. Slim, *Cureus*, 2021, **13**, e13389.
29 M. C. Morris, D. A. Evans, C. C. Tangney, J. L. Bienias, R. S. Wilson, N. T. Aggarwal and P. A. Scherr, *Am. J. Clin. Nutr.*, 2005, **81**, 508–514.
30 M. Lechner, B. Reiter and E. Lorbeer, *J. Chromatogr. A*, 1999, **857**, 231–238.
31 H. Chen, M. Angiuli, C. Ferrari, E. Tombari, G. Salvetti and E. Bramanti, *Food Chem.*, 2010, **125**, 1423–1429.
32 R. Zhang, W. Shen, X. Wei, F. Zhang, C. Shen, B. Wu, Z. Zhao, H. Liu and X. Deng, *Anal. Methods*, 2016, **8**, 7341–7346.
33 M. Sys, B. Svecova, I. Svancara and R. Metelka, *Food Chem.*, 2017, **229**, 621–627.
34 J. Liu and J. Zhang, *Chem. Rev.*, 2020, **120**, 2123–2170.
35 Y. Yang, S. Bernardi, H. Song, J. Zhang, M. Yu, J. C. Reid, E. Strounina, D. J. Searles and C. Yu, *Chem. Mater.*, 2016, **28**, 704–707.
36 Y. Zhan, S. Yang, F. Luo, L. Guo, Y. Zeng, B. Qiu and Z. Lin, *ACS Appl. Mater. Interfaces*, 2020, **12**, 30085–30094.
37 E. C. Le Ru, J. Grand, N. Felidi, J. Aubard, G. Levi, A. Hohenau, J. R. Krenn, E. Blackie and P. G. Etchegoin, *J. Phys. Chem. C*, 2018, **22**, 8117–8812.
38 L. Judith, J. de A. Dorleta, A. Javier, A. A. Ramon, A. Baptiste, J. B. Jeremy and C. B. Guillermo, *ACS Nano*, 2020, **14**, 28–117.
39 S. Y. Ding, E. M. You, Z. Q. Tian and M. Moskovits, *Chem. Soc. Rev.*, 2017, **46**, 4042–4076.
40 E. Seo, S. J. Ko, S. H. Min, J. Y. Kim and B. S. Kin, *Chem. Mater.*, 2015, **27**, 4789–4798.
41 Q. Ding, H. Zhou, H. Zhang, Y. Zhang, G. Wang and H. Zhao, *J. Mater. Chem. A*, 2016, **4**, 8866–8874.
42 S. Zhang, R. Li, X. Liu, L. Yang, Q. Lu, M. Liu, H. Li, Y. Zhang and S. Yao, *Biosens. Bioelectron.*, 2017, **92**, 457–464.
43 H. Cui, G. Hong, X. Wu and Y. Hong, *Mater. Res. Bull.*, 2020, **37**, 2155–2163.
44 W. Zhao, S. Xiao, Y. Zhang, D. Pan, J. Wen, X. Qian, D. Wang, H. Cao, W. He, M. Quan and Z. Yang, *Nanoscale*, 2018, **10**, 14220–14229.